Research Square

Preprints are preliminary reports that have not undergone peer review.
They should not be considered conclusive, used to inform clinical practice,
or referenced by the media as validated information.

Selective catalytic oxidation of methanol on Pt-modified Cu/SSZ-13 zeolites: A strategy to change the catalytic performance by impregnation sequential

Qingliang Zeng
Dalian Maritime University
Zhitao Han
hanzt@dlmu.edu.cn
Dalian Maritime University
Tingjun Liu
Dalian Maritime University
Shoujun Zhang
Guangdong Ocean University
Shaoqin Sheng
Guangzhou Shipyard International Company Ltd
Liangzheng Lin
Dalian Maritime University
Junhao Jing
Dalian Maritime University
Sihan Yin
Dalian Maritime University

Research Article

Keywords: CH3OH-SCO, Cu/Pt/SSZ-13, PtOx, CuO, formate

Posted Date: July 11th, 2025

DOI: https://doi.org/10.21203/rs.3.rs-6991891/v1

License: This work is licensed under a Creative Commons Attribution 4.0 International License.
Read Full License

Additional Declarations: No competing interests reported.

Abstract

The use of methanol as an alternative fuel for marine diesel engines increases unregulated CH_3OH emissions. A series of Pt-modified Cu/SSZ-13 catalysts were prepared using different impregnation method, which selectively catalyzed oxidation of CH_3OH (CH_3OH-SCO) to CO_2 and H_2O. Activity tests showed that Cu/Pt/SSZ-13 catalyst (Pt impregnated first, followed by Cu) displayed exceptional CH_3OH-SCO performance, achieving 100 % methanol conversion at 150 °C with negligible CO and HCHO byproduct formation (< 5 ppm) across the tested temperature range. Additionally, Cu/Pt/SSZ-13 catalyst exhibited excellent SO_2 resistance and high synergistic activity for simultaneous CH_3OH and NO_x removal. Characterization results demonstrated that Cu/Pt/SSZ-13 catalyst exhibited larger pore size, higher specific surface area, abundant strong alkaline site density and elevated surface-adsorbed oxygen (O_{ads}) proportion. It was originated from the preferential introduction of Pt and subsequent doping of Cu enhanced the synergistic interaction at the interface of PtO_x and CuO species, which facilitated the rapid migration of reactive oxygen species, thus accelerating the methanol dehydrogenation and deep oxidation. In-situ DRIFTS results indicated that Cu/Pt/SSZ-13 inhibited the deposition of formate while promoting the rapid conversion of intermediates such as formaldehyde and formic acid to CO_2.

1. Introduction

The utilization of methanol as an alternative fuel in internal combustion engines has gained significant attention due to its carbon-neutral potential and reduced particulate emissions[1]. However, unburned methanol (CH_3OH) in engine exhaust poses environmental and health risks[2]. Selective catalytic oxidation (SCO) was demonstrated as a promising strategy for methanol elimination, enabling the selective oxidation of CH_3OH (CH_3OH-SCO) to CO_2 and H_2O. The core of SCO technology lay in the catalyst, where the design of the catalyst played a pivotal role in determining methanol conversion efficiency and minimizing the production of toxic byproducts (e.g. HCHO, CO).

Cu/SSZ-13 had been commercially deployed for selective catalytic reduction (SCR) denitration in exhaust from heavy-duty vehicles and marine engines, owing to its distinctive CHA topology and high specific surface area[3, 4]. Consequently, researchers prioritized investigations into its application for SCO reactions[5, 6]. The CuO active component exhibited strong oxidation capability, while the SSZ-13 support demonstrated superior CH_3OH adsorption capacity compared to ZSM-5 and Beta zeolites[7, 8]. Nevertheless, Cu/SSZ-13 catalyst suffered from insufficient high-temperature activity and inadequate sulfur resistance during catalytic processes[9]. Platinum-loaded catalysts were reported to exhibit high activity for the oxidation of methanol and carbon monoxide. Mo et al[10]. significantly enhanced the methanol oxidation activity of Pt/MnO_2 catalysts by modifying MnO_2 supports with platinum nanoparticles (NPs), compared to pristine MnO_2. Characterization results revealed that the superior reactivity of Pt/MnO_2 could be attributed to the interfacial interaction between Pt NPs and the MnO_2 support, which modulated the local Pt-Mn coordination environment. It was interaction endowed the

catalyst with enhanced low-temperature reducibility, a high concentration of Mn^{4+} species, and highly active surface lattice oxygen. Tian et al[11]. synthesized platinum-loaded ZSM-5 catalysts for the complete oxidation of CO and C_3H_6. Pt/ZSM-5 catalyst demonstrated strong metal-support interactions between atomically dispersed Pt species and the ZSM-5 framework. The synergistic effects of PtO_x species and Pt-associated lattice oxygen as active centers enabled Pt/ZSM-5 catalyst to achieve complete oxidation with high reaction rates and low activation energy. Notably, despite the exceptional performance of platinum-loaded catalysts, the high cost of platinum remains a critical limitation for their large-scale production and practical application.

Thus, doping Cu/SSZ-13 catalysts with trace platinum had become a reliable alternative strategy to obtain high-performance SCO catalysts. Yu et al[12]. designed a Pt/Cu-SSZ-13 catalyst that exhibited excellent NH_3-SCO performance under realistic conditions with water vapor, achieving 100% conversion at 200–350°C and over 85% N_2 selectivity across the entire tested temperature range. Liu et al[13]. developed a PtCu/SSZ-13 catalyst where PtCu alloy nanoparticles were dispersed on the support surface. In this system, Pt species in the alloyed PtCu nanoparticles existed in an electron-rich state, while electron-deficient Cu and isolated Cu^{2+} species coexisted on the PtCu-SSZ-13 surface. It was unique alloy structure with modulated oxidation states significantly improved the N_2 selectivity of NH_3-SCO over PtCu/SSZ-13 catalyst.

In this study, we adopted a simple impregnation method utilizing SSZ-13 zeolite as a shared substrate for supporting Pt and Cu. By systematically investigating the effects of impregnation sequence, we elucidated their interaction mechanisms on catalyst performance and the oxidation reaction pathways of CH_3OH over the catalyst. This work provides crucial guidance for designing high-efficiency CH_3OH-SCO catalysts with superior activity and minimized byproduct formation.

2. Experimental

2.1 Catalyst preparation

Cu/SSZ-13 and Pt/SSZ-13 catalysts were prepared by impregnation; Pt-Cu/SSZ-13 (co-impregnated with Cu and Pt) catalysts were prepared by co-impregnation; Pt/Cu/SSZ-13 (prepared by sequential impregnation of Cu followed by Pt) and Cu/Pt/SS-13 (Pt impregnated first, followed by Cu) catalysts were prepared by distribution impregnation. The detailed preparation protocols were described in Supporting Information.

2.2 Catalyst activity test

The evaluation of the catalytic activity was displayed in Supporting Information.

2.3 Catalyst characterization

The physical and chemical properties of catalyst samples were characterized with X-ray diffraction (XRD), Scanning electron microscopy (SEM), Energy dispersive X-ray (EDS), N_2 adsorption-desorption, X-ray photoelectron spectra (XPS), Ultraviolet–Visible Diffuse Reflectance Spectroscopy (UV-Vis/DRS), H_2 temperature programmed reduction (H_2-TPR) and CO_2 temperature programmed desorption (CO_2-TPD). The adsorption behavior of gaseous reactants and in-situ CH_3OH-SCO reaction processes were investigated via In-situ Diffuse Reflectance Infrared Fourier Transform Spectroscopy (In-situ DRIFTS) to reveal the possible reaction mechanism. The detailed test conditions were described in Supporting Information.

3. Results and discussion

3.1 CH_3OH-SCO performance

Figure 1(a) displays the CH_3OH conversion of Cu/SSZ-13, Pt/SSZ-13, Pt-Cu/SSZ-13, Pt/Cu/SSZ-13, and Cu/Pt/SSZ-13 catalysts within the temperature range of 100–300°C. As shown in Fig. 1(a), Cu/SSZ-13 catalyst exhibited relatively moderate methanol oxidation performance at low temperatures, with T_{100} (the temperature at which 100% CH_3OH conversion was achieved) of 220°C. The catalytic activity improved for Pt/Cu/SSZ-13 catalyst, which T_{100} was reduced to 200°C. It further confirmed that Pt modification enhanced the catalytic activity of Cu/SSZ-13. After changing the impregnation order, Pt-Cu/SSZ-13 catalyst demonstrated a notably higher performance, with T_{100} of 180°C. Further optimization of impregnation sequence, Cu/Pt/SSZ-13 catalyst resulted in a remarkable improvement, reaching 100% CH_3OH conversion even at a low temperature of 160°C. These findings highlight that the impregnation sequence of Pt and Cu significantly influenced the SCO performance of PtCu/SSZ-13 catalysts. Surprisingly, Pt/SSZ-13 catalyst demonstrated exceptional methanol oxidation performance, maintaining 100% CH_3OH conversion across the entire temperature range of 100–300°C. This superior activity was attributed to the exceptionally strong oxidative capacity of Pt species, which enabled complete low-temperature oxidation of CH_3OH[14].

Figure 1(b) shows the HCHO yields of the five catalysts within the temperature range of 100–300°C. The results indicated that all five catalysts generated small amounts of HCHO byproducts at low temperatures. The HCHO yield order at low temperatures was determined as Pt/Cu/SSZ-13 > Cu/Pt/SSZ-13 > Cu/SSZ-13 > Pt-Cu/SSZ-13 > Pt/SSZ-13. Figure 1(c) shows the CO yields of the five catalysts within the temperature range of 100–300°C. The results indicated that Cu/SSZ-13 catalyst generated the highest CO yield (4.3%) across the entire temperature window, followed by Pt/Cu/SSZ-13 catalyst with a yield of 2.5%. In contrast, virtually no CO production was detected for Pt/SSZ-13, Pt-Cu/SSZ-13, and Cu/Pt/SSZ-13 catalysts throughout the tested temperature range.

The methanol/diesel dual-fuel engine operates in two modes: (1) Diesel mode: Pure diesel was utilized as the sole fuel, analogous to conventional diesel engines. The exhaust characteristics remained consistent with traditional diesel emissions, necessitating aftertreatment systems such as SCR or EGR

(Exhaust Gas Recirculation) to comply with Tier III emission standards. (2) Methanol-dominant mode: Methanol served as the primary fuel (accounting for over 90% of consumption), with diesel acting as the ignition fuel[15–17]. In this mode, the exhaust contained both NO_x and unburned methanol, which exhibited distinct emission profiles compared to conventional diesel engines. While conventional SCR/EGR systems effectively reduced NO_x emissions, the residual methanol required specialized SCO aftertreatment[18]. To address the emission control demands of marine methanol-fueled engines, we hoped that the developed catalysts were based on realizing efficient SCO removal of methanol and also possessing SCR denitrification functions., thus reducing the complexity and cost of after-treatment systems. Consequently, we further investigated the performance of this series of catalysts for the synergistic catalytic removal of methanol and NO_x.

The simultaneous NO_x reduction and CH_3OH oxidation performance of the five catalysts was evaluated under co-feeding conditions of 500 ppm CH_3OH, 500 ppm NH_3, 500 ppm NO_x, 5% O_2, and balanced N_2 within the temperature range of 100–450°C. As shown in Fig. 2(a), all Cu-containing catalysts (Cu/SSZ-13, Pt-Cu/SSZ-13, Pt/Cu/SSZ-13, and Cu/Pt/SSZ-13) exhibited nearly identical methanol removal performance, with T_{100} of 225°C. In contrast, Pt/SSZ-13 catalyst demonstrated significantly weaker CH_3OH oxidation activity, with its T_{100} increasing to 250°C. Notably, compared to its standalone CH_3OH-SCO performance, Pt/SSZ-13 catalyst showed a marked decline in methanol conversion efficiency under simultaneous NO_x reduction and CH_3OH oxidation conditions. It could be attributed to competitive adsorption between NH_3 and CH_3OH on the catalyst surface, which likely suppressed CH_3OH activation and oxidation over Pt/SSZ-13. Figure 2(b) showed the HCHO yields of the five catalysts within the temperature range of 100–450°C. All Pt-containing catalysts (Pt/SSZ-13, Pt-Cu/SSZ-13, Pt/Cu/SSZ-13, and Cu/Pt/SSZ-13) generated minimal HCHO (< 5 ppm) only at low temperatures (100–150°C). In contrast, Cu/SSZ-13 catalyst exhibited nearly 100% HCHO yield in the 100–200°C range, indicating that CH_3OH was predominantly oxidized to HCHO at low temperatures over this catalyst. Figure 2(c) displayed the CO yields of the five catalysts across the same temperature range. All catalysts produced negligible CO (< 5 ppm) only between 200–250°C. The results demonstrate that under simultaneous NH_3, NO_x, and CH_3OH co-feeding conditions, Pt-Cu/SSZ-13, Pt/Cu/SSZ-13, and Cu/Pt/SSZ-13 catalysts exhibited superior SCO performance.

Figure 2(d) showed the NO_x conversion efficiencies of the five catalysts within the temperature range of 100–450°C. Cu/SSZ-13 catalyst exhibited 100% across a broad temperature window of 185–329°C. After modifying Cu/SSZ-13 with Pt via impregnation to form Pt/Cu/SSZ-13, the denitration performance slightly declined, achieving ~ 100% NO_x conversion within a window of 194–316°C. Modifying the impregnation sequence, both Pt-Cu/SSZ-13 and Cu/Pt/SSZ-13 catalysts showed a low-temperature shift in their active windows, with nearly identical NO_x conversion profiles (~ 100% within 191–314°C). In contrast, Pt/SSZ-13 catalyst demonstrated a much narrower active window (246–279°C). Figure 2(e) presented the N_2 selectivity of the five catalysts over the same temperature range. The N_2 selectivity trends mirrored the NO_x conversion performance, following the order: Cu/SSZ-13 > Pt/Cu/SSZ-13 >

Cu/Pt/SSZ-13 ≈ Pt-Cu/SSZ-13 > Pt/SSZ-13. Notably, the Pt/SSZ-13 catalyst exhibited anomalously low N_2 selectivity (-17%), which was attributed to the over-oxidation of NH_3 to N_2O by highly oxidative Pt species, resulting in negative selectivity[19]. These results confirmed that Cu-containing catalysts demonstrated superior SCR performance under simultaneous NH_3, NO_x, and CH_3OH co-feeding conditions, achieving both high NO_x conversion efficiency and favorable N_2 selectivity.

Based on the results of CH_3OH-SCO and simultaneous NO_x-Methanol removal, Cu/Pt/SSZ-13 catalyst prepared through sequential impregnation demonstrated dual functionality: (1) exhibited excellent selective catalytic oxidation (SCO) activity at low temperatures, maintaining a CH_3OH conversion rate exceeding 100% across a broad temperature window of 150–300°C; (2) displayed satisfactory SCR performance. Therefore, Cu/Pt/SSZ-13 catalyst will be selected in the following as the main study for subsequent CH_3OH-SCO characterization and analysis. Notably, while the Pt/SSZ-13 catalyst showed superior CH_3OH-SCO activity, its practical application in methanol/diesel dual-fuel engines remained unsuitable due to insufficient SCR performance. Consequently, Pt/SSZ-13 served solely as a control catalyst in this study to elucidate the mechanistic impacts of impregnation sequence on Pt-modified Cu/SSZ-13 catalysts during SCO processes.

3.2 Structural and textural characteristics

3.2.1 XRD

Figure 3 shows the XRD characterization results of the synthesized catalysts. Clear diffraction peaks corresponding to the chabazite (CHA) structure of SSZ-13 zeolite were clearly observed for all catalysts, indicating that neither the stepwise nor co-impregnation methods, nor the incorporation of transition or noble metals, disrupted the zeolitic framework[20]. It confirmed the strong structural stability of SSZ-13 zeolite. High-resolution magnification was performed on regions associated with CuO and Pt species. A weak diffraction peak at 38.7 ° was detected in all Cu-containing catalysts, which was attributed to CuO species, suggesting the formation of small-sized CuO crystallites on their surfaces[21]. Similarly, diffraction peaks related to the Pt (111) plane were observed in all Pt-containing catalysts, but with very low intensity. It could be attributed to the low Pt loading or the uniform distribution of Pt species without significant aggregation[22].

3.2.2 TEM and EDS

TEM and EDS images of Cu/SSZ-13 (a), Pt/SSZ-13 (b), Pt-Cu/SSZ-13 (c), Pt/Cu/SSZ-13 (d), and Cu/Pt/SSZ-13 (e) catalysts are shown in Figs. 4 and 5, respectively. CuO clusters smaller than 2 nm were uniformly distributed on the surface of Cu/SSZ-13 catalyst and the Cu elements were well dispersed[23]. For Pt/SSZ-13 catalysts, metallic Pt and PtO_x species with a lattice spacing of about 0.2 nm were observed on the surface. It indicated that in the Pt-containing catalysts (Pt/SSZ-13, Pt-Cu/SSZ-13, Pt/Cu/SSZ-13, Cu/Pt/SSZ-13), Pt mainly existed as metallic Pt and PtO_x on the surface of the carriers or at the entrance of the zeolite pores. In addition, EDS results further verified the high dispersion of Pt species[24]. For Pt-Cu/SSZ-13 catalyst, some agglomerates due to uneven metal distribution were

observed on the surface, which was related to the simultaneous competition of Pt and Cu precursors for the adsorption sites of the carrier. It was hypothesized by EDS mapping that the agglomerates might be the oxide species of Pt and Cu in the form of massive clusters. Pt/Cu/SSZ-13 catalyst boundaries showed a large number of species with inhomogeneous sizes, which may be mainly Pt-CuO composites formed by Pt species in amorphous state and a small number of CuO clusters[25]. It suggested that the preferential impregnation of Cu with higher loading blocked the microporous entrances or internal channels, which led to the ineffective dispersion of the subsequent Pt impregnation, thus further aggravating the pore blockage. When Cu/Pt/SSZ-13 catalyst was impregnated with Pt first, its precursors preferentially occupied the high-affinity sites on the surface of the SSZ-13 carrier, which provided nucleation centers for the subsequently impregnated Cu and inhibited the aggregation of Cu particles. It was noteworthy that the outer surface of Cu/Pt/SSZ-13 catalyst showed large particles in the form of clumps, which could be hypothesized to be the clumps formed by PtO_x and CuO species in combination with the EDS patterns. It was due to the excessive Cu loading, some Cu elements aggregated on the outer surface of the zeolite, the formation of massive CuO species after high temperature calcination, and the formation of Pt-Cu nanocrystals from some Pt species on the surface of SSZ-13 and massive CuO during the process of secondary impregnation. However, such Pt-Cu nanoclusters were mainly embedded in the outer surface of the catalyst and had minimal effect on the active sites on the surface or inside the catalyst zeolite[26].

3.2.3 BET

The surface physical properties of the synthesized catalysts were investigated via N_2 adsorption-desorption experiments, with the results shown in Fig. 6. All catalysts exhibited Type I isotherms, characteristic of microporous materials[27]. Table. 1 summarizes the specific surface areas, micropore areas, average pore diameter, and pore volumes of the catalysts. The order of specific surface area and microporous area size was Pt/SSZ-13 > Cu/Pt/SSZ-13 > Pt/Cu/SSZ-13 > Pt-Cu/SSZ-13 > Cu/SSZ-13, and the pore volume and pore diameter were in the following order: Cu/SSZ-13 > Cu/Pt/SSZ-13 > Pt-Cu/SSZ-13 > Pt/SSZ-13 > Pt/Cu/SSZ-13. Pt/SSZ-13 catalyst exhibited a high specific surface area (566.5 m^2/g), suggesting that low-loading Pt was dispersed on the support surface via strong interactions with active sites ($Si\text{-}O\text{-}Al^-$)[28]. Cu/SSZ-13 catalyst displayed a lower specific surface area and micropore area due to severe Cu aggregation and pore blockage at high Cu loadings. For Pt/Cu/SSZ-13 catalyst, the high Cu loading nearly completely blocked the micropores, and subsequently impregnated Pt primarily existed in an oxidized state (PtO_x) on the catalyst surface. It indicated that PtO_x species could promote Cu dispersion, thereby alleviating micropore blockage. Consequently, the specific surface area and micropore area of Pt/Cu/SSZ-13 catalyst increased compared to Cu/SSZ-13. When the impregnation sequence was altered (Pt-Cu/SSZ-13, co-impregnation), the specific surface area and micropore area slightly decreased relative to Pt/Cu/SSZ-13, implying that competitive adsorption between Pt and Cu precursors during co-impregnation weakened Pt's inhibitory effect on Cu aggregation[29]. Optimizing the impregnation sequence, the specific surface area, pore volume and pore size of Cu/Pt/SSZ-13 catalysts impregnated with Pt first and Cu later were significantly enhanced. This improvement was attributed to

the preferential dispersion of PtO_x species on the support surface during the initial impregnation step, forming highly dispersed nanoparticles. Subsequently deposited CuO clusters covered the Pt species, while the strong anchoring effect of Pt suppressed Cu agglomeration, reducing metal particle size and mitigating micropore blockage[30].

In summary, among Pt-modified Cu/SSZ-13 catalysts with different impregnation sequences, the adoption of the order of preferential impregnation of Pt followed by Cu impregnation could result in Cu/Pt/SSZ-13 catalyst having larger pore diameters, higher specific surface areas and microporous areas at the same time, which could expose more active sites and exhibit excellent adsorption and catalytic abilities.

Table 1
BET surface area and pore structure results of prepared catalysts.

Catalysts	S_{BET} (m^2/g)	Micropore Area (m^2/g)	Average pore Diameter (nm)	Pore Volume (cm^3/g)
Cu/SSZ-13	461.4	434.5	2.578	0.228
Pt/SSZ-13	566.5	539.1	2.290	0.042
Pt-Cu/SSZ-13	475.3	449.6	2.375	0.045
Pt/Cu/SSZ-13	488.3	459.5	2.283	0.038
Cu/Pt/SSZ-13	516.6	505.9	2.508	0.068

3.2.4 UV-Vis/DRS

UV-vis/DRS analysis of the prepared catalysts was carried out to investigate the chemical state of catalyst surface ions and the results were shown in Fig. 7. For Cu-containing catalysts, the two peaks observed in the wavelength range of 200–300 nm were likely associated with charge transfer from stable Cu^+ and isolated Cu^{2+} ions to O^{2-}, suggesting partial incorporation of Cu^+ and Cu^{2+} ions within the SSZ-13 zeolite framework[31]. The broad band at 600–800 nm corresponded to the d-d orbital transition of Cu^{2+} ions induced by CuO species[32, 33]. In the case of Pt-containing catalysts, the peak appearing between 300–350 nm was attributed to charge transfer in PtO_x species[34]. Among the five investigated samples, Cu/Pt/SSZ-13 exhibited significantly higher intensities for all five characteristic signals compared to other catalysts, indicating substantial coexistence of PtO_x, Cu^+, Cu^{2+}, and CuO species when adopting the sequential impregnation of Pt followed by Cu. It was observation suggested that the synergistic interaction between Pt and Cu species played a critical role in enhancing SCO performance of various Pt-modified Cu/SSZ-13 catalysts.

3.2.4 XPS

To investigate the surface elemental valence states of Pt-modified Cu/SSZ-13 catalysts with different impregnation sequences, XPS analysis was conducted on the synthesized catalysts, as shown in Fig. 8. The surface relative contents of Cu and O elements were determined through integral calculations of their characteristic peaks, with results summarized in Table. 2.

As shown in Fig. 8(a), the Pt *4d* spectra of Pt-containing catalysts were deconvoluted into two sub-peaks. The higher binding energy peak at ~ 333 eV was assigned to oxidized Pt species (Pt^{2+} or PtO_x) [35]. For Pt/SSZ-13, PtO_x species exhibited a highly dispersed state, resulting in an elevated binding energy of 333.59 eV. Pt/Cu/SSZ-13 catalyst displayed the lowest binding energy, implying electron enrichment at Pt sites induced by preferential Cu loading, where Cu likely acted as an electron donor to reduce the oxidation state of Pt[36]. Pt-Cu/SSZ-13 led to a higher binding energy, which might correlate with metal agglomeration. Competition between Pt and Cu precursors for active sites during impregnation promoted particle growth, thereby decreasing the d-orbital electron density of Pt[37]. For the optimized Cu/Pt/SSZ-13 catalyst, the binding energy was intermediate between Pt/SSZ-13 and Pt/Cu/SSZ-13, suggested that subsequent Cu overlayers only partially modified the electronic structure of pre-loaded Pt. This Cu overlayer likely optimized the adsorption strength of SCO reaction intermediates (e.g., formaldehyde, formic acid) by tuning the d-band center of Pt, thereby enhancing catalytic selectivity[38]. Notably, all Pt-containing catalysts exhibited a lower binding energy peak at ~ 316 eV, corresponding to metallic Pt^0, indicating partial reduction during calcination or pretreatment. The minor binding energy shifts ($\Delta BE < 0.8$ eV) among Pt^0 signals implied weak Pt-Cu interactions dominated by physical coexistence or subtle electronic effects rather than strong alloying[37].

As shown in Fig. 8(b), the Cu *2p* spectra of Cu-containing catalysts showed peaks at ~ 935.3 eV and 955.8 eV with satellite features, characteristic of surface Cu^{2+} species (CuO). Peaks at ~ 933.9 eV and 953.5 eV were attributed to Cu^0 and Cu^+[39]. In Pt-Cu/SSZ-13, competition between Pt and Cu precursors for active sites favored CuO formation (64.4% Cu^{2+}). For Pt/Cu/SSZ-13, pre-loaded Cu occupied high-affinity sites in SSZ-13, forcing subsequent Pt deposition onto suboptimal external sites and generating partially reduced Cu species (Cu^0 clusters), which decreased the Cu^{2+} proportion to 61.7%. The strong anchoring effect of Pt in Cu/Pt/SSZ-13 stabilized Cu^+ species (Cu_2O) via electronic interactions, yielding the lowest Cu^{2+} content (56.2%).

The surface oxygen species significantly influenced the redox properties of the catalysts. Figure 8(c) displayed the O *1s* XPS spectra of the five catalysts. Through spectral deconvolution, two distinct oxygen species were identified on the catalyst surfaces: the higher binding energy peak corresponded to chemisorbed oxygen species (O^{2-} or O^-, denoted as O_{ads}), while the lower binding energy peak was attributed to lattice oxygen (O^{2-}, denoted as O_{latt}). O_{ads} participated more readily in redox reactions compared to O_{latt}, which remained tightly bound within the zeolite framework[40]. Consequently, a higher O_{ads} / (O_{ads} + O_{latt}) ratio correlated with enhanced redox activity. As summarized in Table. 2, among the three Pt-modified Cu/SSZ-13 catalysts prepared with different impregnation sequences, Cu/Pt/SSZ-13

exhibited the highest surface-adsorbed oxygen ratio (91.4%). It could be attributed to PtO_x anchoring at high-energy surface sites, which enhanced oxygen mobility, reduced oxygen vacancy formation energy, and facilitated oxygen activation, collectively improving redox capability[41, 42].

Table. 2. XPS data of all catalysts.

Samples	The relative molar ratio (%)	
	Cu^{2+} / (Cu^0+Cu^+)	O_{ads} / (O_{ads}+O_{latt})
Cu/SSZ-13	57.4	93.6
Pt/SSZ-13	-	88.2
Pt-Cu/SSZ-13	64.4	90.6
Pt/Cu/SSZ-13	61.7	89.4
Cu/Pt/SSZ-13	56.2	91.4

3.3 Redox properties

3.3.1 O_2-TPD

O_2-TPD analysis was conducted to investigate oxygen species in the five catalysts, with results shown in Fig. 9. The O_2 desorption peaks in the 200–500°C range were attributed to O_{ads}, while those in the 500–900°C range corresponded to O_{latt}. All catalysts exhibited significantly higher intensity for surface-adsorbed oxygen than lattice oxygen. Previous studies reported that adsorbed oxygen species (e.g., O^-, O_2^-) directly interact with methanol or its intermediates (e.g., CO*, $HCOO^-$), facilitating C-H bond

cleavage and complete oxidation to CO_2, suggesting the dominant role of adsorbed oxygen in methanol catalytic oxidation[43].

The desorption peaks of O_{ads} shifted to lower-temperature regions in the order: Pt/SSZ-13 > Pt-Cu/SSZ-13 ≈ Pt/Cu/SSZ-13 ≈ Cu/Pt/SSZ-13 > Cu/SSZ-13, indicating faster reaction kinetics of adsorbed oxygen on Pt-containing catalysts. Furthermore, although Pt-modified Cu/SSZ-13 catalysts with different impregnation sequences showed nearly identical peak positions for adsorbed oxygen, their relative abundance (calculated via curve integration) ranked in descending order: Cu/Pt/SSZ-13 > Pt-Cu/SSZ-13 > Pt/Cu /SSZ-13. The sequential impregnation strategy optimized both oxygen mobility and active site distribution, explaining the superior SCO performance of Cu/Pt/SSZ-13 observed in catalytic testing. These observations aligned with XPS results.

3.3.1 H_2-TPR

The redox properties of the five catalysts were investigated via H_2-TPR experiments, with the results shown in Fig. 10 and Table. 3. For Pt/SSZ-13 catalyst, two weak peaks were observed: the first peak was attributed to the reduction of minor isolated Pt^{2+} ions exchanged within zeolite channels; the second peak corresponded to the reduction of PtO_x species to metallic Pt^0, which likely resided on the zeolite surface or near 6-membered ring (6-MR) pore entrances[28]. In Cu/SSZ-13, Pt/Cu/SSZ-13, Cu/Pt/SSZ-13, and Pt-Cu/SSZ-13 catalysts, four distinct reduction peaks were identified: Peak 1: Reduction of isolated Cu^{2+} ions near 8-membered ring (8-MR) windows and within CHA cages. Peak 2: Single-step reduction of CuO clusters to metallic Cu^0. Peak 3: Reduction of Cu^{2+} species localized near or at 6-MR pore entrances[44]. Peak 4: reduction of minor PtO_x species to metallic Pt^0.

Intriguingly, the total H_2 consumption of Pt/SSZ-13 and Cu/SSZ-13 catalysts showed an inverse correlation with their CH_3OH-SCO activities, suggesting that total reducibility alone was not the decisive factor for methanol oxidation performance[45]. Notably, Cu/Pt/SSZ-13 catalyst showed significantly stronger H_2 consumption for the reduction peaks corresponding to CuO and PtO_x compared to Pt/Cu/SSZ-13 and Pt-Cu/SSZ-13. It was observation indicated enhanced synergistic catalytic oxidation of methanol by CuO and PtO_x species in Cu/Pt/SSZ-13. The optimized synergy accounted for the superior CH_3OH-SCO performance of Cu/Pt/SSZ-13, where Pt^{2+} facilitated the activation of CuO, while CuO stabilized Pt in an oxidized state critical for methanol C-H bond cleavage. The sequential Pt-then-Cu impregnation strategy enabled spatial and electronic coupling between Pt and Cu species, establishing a hierarchically structured active site system that maximized oxygen migration efficiency during catalytic cycles. These findings revealed that PtO_x-CuO interfacial interaction served as the key driving force for complete methanol oxidation.

Table 3
H_2-TPR data of $Cu_{2.5}$/SSZ-13, Cu_{10}/SSZ-13 and $Cu_{12.5}$/SSZ-13 catalysts

Samples	H_2 consumption (mmol / g)				
	Peak 1	Peak 2	Peak 3	Peak 4	Total
Cu/SSZ-13	0.84	1.30	0.37	-	2.56
Pt/SSZ-13	0.19	0.65	-	-	0.84
Pt-Cu/SSZ-13	0.61	0.70	0.72	0.11	2.14
Pt/Cu/SSZ-13	0.55	0.64	0.05	-	1.24
Cu/Pt/SSZ-13	0.71	0.88	0.36	0.32	2.27

3.4 Surface acidity

3.4.1 CO_2-TPD

The surface basicity of the synthesized catalysts was investigated via CO_2-TPD experiments to evaluate the effects of impregnation sequences on Pt-modified Cu/SSZ-13 catalysts, with results shown in Fig. 11. The quantitative analysis of the total alkalinity on the catalyst surface was calculated from the integration of the CO_2-TPD curve and the results are listed in Table 4. All catalysts exhibited desorption peaks in the 100–350°C and 350–600°C temperature ranges. Based on prior reports, the low-temperature peak (< 350°C) was attributed to weak basic sites corresponding to CO_2 desorption from hydrated hydroxyl groups. The CO_2 desorption peaks above 350°C were attributed to strongly basic sites, corresponding to the desorption of CO_2 adsorbed on the free hydroxyl groups on the catalyst surface[46]. Monometallic Pt/SSZ-13 and Cu/SSZ-13 catalysts primarily displayed weak basicity. In contrast, bimetallic catalysts showed enhanced peaks for strong basic sites but significantly reduced total basicity compared to monometallic counterparts, suggesting competitive or synergistic interactions between Pt and Cu species that altered hydroxyl group distributions. Notably, Pt-modified Cu/SSZ-13 catalysts with different impregnation sequences exhibited comparable total basicity. Among them, Cu/Pt/SSZ-13 catalyst demonstrated the highest concentration of strong basic sites (0.3 mmol/g). This increased population of strong basic sites likely facilitated methanol activation via C-H bond polarization, thereby enhancing SCO performance[47, 48]. The sequential Pt-then-Cu strategy optimized the balance between acidic and basic sites, favoring the formation of stable reaction intermediates during CH_3OH oxidation.

Table 4
CO_2-TPD results of all catalysts.

Catalysts	Acid amount (mmol/g)		Total acidity (mmol/g)
	Peak ①	Peak ②	
Cu/SSZ-13	0.77	0.07	0.84
Pt/SSZ-13	0.46	0.03	0.49
Pt-Cu/SSZ-13	0.12	0.32	0.44
Pt/Cu/SSZ-13	0.18	0.22	0.4
Cu/Pt/SSZ-13	0.09	0.35	0.44

3.5. Experimental In-situ DRIFTS

3.5.1 Catalyst preparation Adsorption of $CH_3OH + O_2$

In-situ DRIFTS experiments of $CH_3OH + O_2$ co-adsorption on Cu/Pt/SSZ-13 catalyst was conducted to investigate the types of methanol-derived species adsorbed on the catalyst surface at different temperatures, as shown in Fig. 12. A negative peak at 3668 cm^{-1} corresponded to the O-H stretching vibration of surface hydroxyl groups[49]. Characteristic peaks near 2959 cm^{-1} and 2846 cm^{-1} were attributed to C-H stretching vibrations of methanol and methoxy (CH_3O^-) species, respectively[50]. The peak at 2154 cm^{-1} aligned with gaseous CO_2 formation, while the feature at 2129 cm^{-1} originated from adsorbed CO[51]. Peaks at 1678 cm^{-1} and 1655 cm^{-1} were assigned to C = O stretching vibrations of aldehyde (-CHO) and formic acid (HCOOH) species, respectively[52]. The diminishing intensity of formic acid-related peaks suggested rapid decomposition of formate intermediates or direct oxidation of formaldehyde to CO_2, bypassing intermediate stages. The peak near 1585 cm^{-1} arose from asymmetric O-C-O stretching of carboxylate (COO^-) species, while the feature at 1470 cm^{-1} corresponded to symmetric O-C-O stretching of formate ($HCOO^-$) intermediates, both critical in methanol oxidation pathways[53]. The emergence of a carbonate (CO_3^{2-}) peak at 1509 cm^{-1} at 200°C indicated deep oxidation of methanol[53]. A prominent peak at 1295 cm^{-1} represented C-O stretching of methanol, while features near 1250 cm^{-1} and 1120 cm^{-1} were linked to C-O vibrations of methoxy (CH_3O^-) species[54]. The progressive enhancement of CH_3O^--related peaks across 50–350°C demonstrated the persistent involvement of methoxy species throughout the SCO reaction. This observation implied that Pt doping facilitated direct dehydrogenation of methanol to methoxy species, rather than relying on surface hydroxyl groups or oxygen vacancies. Such a pathway shortened the reaction route, enabling rapid methanol removal at low temperatures.

In-situ DRIFTS experiments were conducted to investigate the transient CH_3OH-SCO reaction of co-adsorbed CH_3OH and O_2 on the Cu/Pt/SSZ-13 catalyst at 200°C, with results shown in Fig. 13. As shown in Fig. 13(b), the peak intensities attributed to methanol species in the in-situ spectra of Pt/Cu/SSZ-13 catalyst gradually increased with reaction time (1–60 min), indicating that the catalyst continued to adsorb methanol at 200°C, which implied insufficient adsorption functionality. From Fig. 13, the peaks corresponding to methoxy and formate species progressively intensified for all three catalysts as the reaction time increased, further confirming that methoxy and formate were key intermediates in the CH_3OH-SCO reaction.

Notably, Cu/Pt/SSZ-13 catalyst exhibited weaker formate-related peaks, suggesting that it partially bypassed the formate generation stage, thereby suppressing formic acid accumulation and directly promoting complete methanol oxidation to CO_2. The rapid enrichment of methoxy and formate species indicated that the reaction pathway predominantly followed a direct dehydrogenation-oxidation mechanism, rather than sequential carboxylate-mediated steps. It was behavior aligned with the catalyst's high low-temperature SCO efficiency, as suppressing formate accumulation minimized intermediate poisoning and accelerated overall reaction kinetics. The Pt-first impregnation sequence enhanced the synergy between Pt (facilitating C-H bond cleavage) and CuO (enhancing oxygen mobility), thereby enabling this simplified reaction pathway[55, 56].

3.5.2 Discussion on reaction mechanism

Proposed Methanol Catalytic Oxidation Pathway (Based on In Situ DRIFTS)

Step 1: Methanol Adsorption and Dehydrogenation

The high dehydrogenation activity of Pt accelerated methanol conversion to methoxy species, while the synergy between Cu and Pt synergistically catalyzed the reaction, lowering the activation energy.

$CH_3OH \rightarrow CH_3O^- + H^+$

Step 2: Rapid Methoxy - to - Formaldehyde Conversion

Pt promoted surface oxygen activation ($O_2 \rightarrow 2O^-$), facilitating methoxy dehydrogenation.

$CH_3O^- \rightarrow HCHO + H^+$

Step 3: Efficient Formaldehyde - to - Formic acid Conversion

Formaldehyde reacted with surface hydroxyl groups to form formic acid, which subsequently dissociated into formate species.

$HCHO + H_2O \rightarrow HCOOH$

$HCOOH \rightarrow HCOO^- + H^+$

Step 4: Rapid Decomposition of Formate

Pt's strong oxidizing ability inhibited formate accumulation and promoted its rapid conversion to CO_2.

$HCOO^- + 1/2\ O_2 \rightarrow CO_2 + H_2O + e^-$

Parallel Pathways:

CO Oxidation: Pt preferentially adsorbed and rapidly oxidized CO.

$CO + O^- \rightarrow CO_2$

Enhanced Carbonate Decomposition: Strong Pt-Cu interfacial interactions promoted CO_3^{2-} decomposition.

$CO_3^{2-} \rightarrow CO_2 + O_2^-$

4. Conclusion

Cu/Pt/SSZ-13 catalyst, prepared by sequential impregnation (Pt first, Cu second), selectively oxidized methanol to CO_2 and H_2O at 160°C with minimal byproduct formation, thereby effectively controlling CH_3OH emissions from methanol-fueled engines. Additionally, Cu/Pt/SSZ-13 catalyst demonstrated excellent SO_2 resistance and maintained high activity during simultaneous denitration and methanol removal, highlighting its potential as a multifunctional catalyst. Characterization studies revealed that Pt was preferentially dispersed on the carrier surface in the form of PtO_x species. Meanwhile, the strong anchoring effect of Pt promoted the uniform dispersion of the subsequently introduced small-sized CuO nanoclusters. The rational distribution of Pt and Cu species endowed the Cu/Pt/SSZ-13 catalyst with a larger pore size and higher specific surface area, providing ideal pathways for reactant diffusion and intermediate conversion. Furthermore, the Cu/Pt/SSZ-13 catalyst exhibited a high density of strong alkaline sites and an elevated proportion of surface-adsorbed oxygen, which originated from the synergistic interfacial effects between PtO_x and CuO species. It was synergy facilitated the rapid generation of active oxygen species, accelerating methanol dehydrogenation and deep oxidation. In situ DRIFTS results confirmed that Cu/Pt/SSZ-13 catalyst suppressed the deposition of formate intermediates while promoting the rapid conversion of formaldehyde intermediates to CO_2. This study demonstrated the efficient methanol removal performance of a cost-effective Pt-modified Cu/SSZ-13 catalyst, which provides a new strategy for designing CH_3OH-SCO catalysts that can effectively reduce CH_3OH emissions from methanol/diesel engines while minimizing undesirable by-products during CH_3OH oxidation.

Abbreviations

SCO Selective catalytic oxidation

CH_3OH-SCO selectively catalyzed oxidation of CH_3OH

NH_3-SCO Selective catalytic oxidation of ammonia

XRD X-ray diffraction

SEM Scanning electron microscopy

EDS Energy dispersive X-ray

XPS X-ray photoelectron spectra

UV-Vis/DRS Ultraviolet–Visible Diffuse Reflectance Spectroscopy

H_2-TPR H_2 temperature programmed reduction

CO_2-TPD CO_2 temperature programmed desorption

In-situ DRIFTS In-situ Diffuse Reflectance Infrared Fourier Transform Spectroscopy

SCR selective catalytic reduction

NPs nanoparticles

EGR Exhaust Gas Recirculation

CHA chabazite

Declarations

Acknowledgments

The authors gratefully acknowledge for the financial support from the Guangdong Province Natural Resources Project (2022-32) and the National Natural Science Foundation of China (52271356).

Author Contributions

Qingliang Zeng: Conceptualization, Methodology, Formal analysis, Data curation, Writing-original & draft. Zhitao Han: Methodology, Writing-review & editing, Project administration, Funding acquisition. Tingjun Liu: Investigation, Resources. Shoujun Zhang: Investigation, Resources. Shaoqin Sheng: Investigation, Resources. Liangzheng Lin: Investigation, Resources. Junhao Jing: Investigation, Resources. Sihan Yin: Investigation, Resources.

Funding

This work was supported by Guangdong Province Natural Resources Project (2022-32), National Natural Science Foundation of China (52271356).

Data Availability

No datasets were generated or analysed during the current study.

Competing Interests The authors declare no competing interests.

Ethics and Consent to Participate Not applicable.

Consent for Publication Not applicable.

References

1. Tian Z, Wang Y, Zhen X, Liu Z (2022) Fuel 320:123902.
2. Ma B, Yao A, Yao C, Wang W, Ai Y (2021) Appl Energy 300:117355.
3. Mohan S, Dinesha P, Kumar S (2020) Chem Eng J 384:123253.
4. Wang Y, Zhu T, Zhao Y, Hao X (2024) J. Chin Chem Soc. 71:1448-1463.
5. Jabłońska M (2020) ChemCatChem 12:4490-4500.
6. Cheng S, Han Z, Xu D, Li Y, Tian Y, Zeng Q, Lu S (2024) Process Saf Environ 181:33-42.
7. Zhou L, Günther S, Moszynski D, Imbihl R (2005) J Catal 235:359-367.
8. Guo X, Li D, Wang L, Deng H, Wang Y, Wang H, Ma J, Yu Y, He H (2025) Sep Purif Technol 361:131634.
9. Jabłońska M (2022) RSC Adv 12:25240-25261.
10. Ru X, Li W, Wang X, Shi Z, Wen X, Mo S, Mo D (2023) Chem Eng Sci. 281:119079.
11. Daniel S, Monguen CKF, Ayodele OB, Tian ZY (2023) J Environ Chem Eng 11:109617.
12. An Q, Xu G, Liu J, Wang Y, Yu Y, He H (2023) ACS Catal 13:6851-6861.
13. Yao P, Li J, Pei M, Liu F, Xu H, Chen Y (2024) ACS Appl Mater Interfaces 16:14694-14703.
14. Jiang Z, Liu J, Ruan H, Jia Y, Qian H, Deng W, Guo L (2024) J Environ Chem Eng 12:113217.
15. Wei H, Yao C, Pan W, Han G, Dou Z, Wu T, Liu M, Gao J, Chen C, Shi J (2017) Fuel 207:33-46.
16. Qu G, Yao A, Chen C, Ren J, Yao C (2021) Fuel 299:120879.
17. Ni P, Wang X, Li H (2020) Fuel 279:118477.
18. Liu J, Liang W, Ma H, Ji Q, Xiang P, Sun P, Wang P, Wei M, Ma H (2023) Energy 282:128819.
19. Zhao Y, Yi X, Dou B, Kang R, Bin F (2024) ACS Appl Mater Interfaces 16:26088-26098.
20. Pappas DK, Borfecchia E, Dyballa M, Pankin IA, Lomachenko KA, Martini A, Signorile M, Teketel S, Arstad B, Berlier G (2017) Am Chem Soc 139:14961-14975.
21. Sun H, Wang H, Qu Z (2023) ACS Catal 13:1077-1088.

22. Ou L (2018) ACS omega 3:886-897.
23. Zhang H, Lv J, Zhang Z, Du C, Wang S, Lin J, Wan S, Wang Y, Xiong H (2022) ChemCatChem 14:e202101609.
24. Cheng S, Han Z, Zhao H, Li Y, Lu S (2024) Chem Eng J 479:147876.
25. Olofsson G, Wallenberg LR, Andersson A (2005) J Catal 230:1-13.
26. Zhao S, Lin J, Gong W, Xu A, Li X, Qiu Y (2024) Sep Purif Technol 332:125864.
27. Wang J, Shao L, Wang C, Wang J, Shen M, Li W (2018) J Catal 367:221-228.
28. Li Y, Ma Y, Wei Y, Liang P, Yu Y, Pei W, Sun T (2024) J Chem Phys 161.
29. Wang Z, Zhao Q, Tan M, Qu D, Chen B, Shi C (2025) Appl Catal B Environ 125107.
30. Hua-Yan Z, Tian-Yu G, Zhong L, Fan-Hui M, Yao Q (2013) Chin J Inorg Chem 29:2575-2581.
31. Pestryakov AN, Petranovskii VP, Kryazhov A, Ozhereliev O, Pfänder N, Knop-Gericke A (2004) Chem Phys Lett 385:173-176.
32. Liang C, Li X, Qu Z, Tade M, Liu S (2012) Appl Surf Sci 258:3738-3743.
33. Lezcano-Gonzalez I, Deka U, Van Der Bij H, Paalanen P, Arstad B, Weckhuysen B, Beale A (2014) Appl Catal B Environ 154:339-349.
34. Xiong Z, Wang H, Xu N, Li H, Fang B, Zhao Y, Zhang J, Zheng C (2015) Int J Hydrog Energy 40:10049-10062.
35. Hu S, Huang M, Li J, He J, Xu K, Rao X, Cai D, Zhan G (2023) Appl Catal B Environ 333:122804.
36. Jia L, Shao Y, Li Z, Li K, Ren X, Wu H, Li H, Cheng K, Cheng H, Liu J (2024) ACS EST Engg 4:1007-1015.
37. Sun G, Zhao Z-J, Mu R, Zha S, Li L, Chen S, Zang K, Luo J, Li Z, Purdy SC (2018) Nat Commun 9:4454.
38. Wang P, Liao H, Chen Y, Tao X, Gan Y, Deng H, Fu Y, Tang Y, Wu L, Tan L (2024) ACS Catal 14:8116-8129.
39. Guo J, Yang W, Zhang Y, Gan L, Fan C, Chen J, Peng Y, Li J (2020) Catal Commun 135:105751.
40. Zhao Y, Yi X, Dou B, Zhang C, Zhao Z, Bin F (2024) Sep Purif Technol 349:127727.
41. Tang T, Zhao S, Liu Y, Tang X, Sun L, Ma Y, Zhu R, Yi H (2024) J Hazard Mater 480:135839.
42. Li Cf, Guo Rt, Zhang Zr, Wu T, Pan Wg (2023) Small 19:2207875.
43. Yun J, Lee S, Bae D, Kim M (2024) Korean J Chem Eng 1-10.
44. Zhou W, Wang F, He N, Yu H, Ma X, Liu J (2022) CIESC J 73:672.
45. Li C, Han Z, Hu Y, Liu T, Pan X (2022) RSC Adv 12:27309-27320.
46. Nagpure AS, Mohture VM, Kayarkar A (2022) Inorg Chem Commun 146:110118.
47. Wang Z, Zhao Q, Tan M, Qu D, Chen B, Shi CJACBE (2025) Energy 125107.
48. Gao J, Boahene PE, Hu Y, Dalai A, Wang H (2019) Catalysts 9:922.
49. Xu Z, Mo S, Li Y, Zhang Y, Wu J, Fu M, Niu X, Hu Y, Ye D (2022) Chemosphere 286:131754.
50. Chen S, Ma X (2017) Ind Eng Chem 45:296-300.

51. Wang X, Arvidsson AA, Cichocka MO, Zou X, Martin NM, Nilsson J, Carlson S, Gustafson J, Skoglundh M, Hellman A (2017) Phys Chem C 121:27389-27398.
52. Ma L, Seo CY, Chen X, Li J, Schwank JW (2018) Chem Eng J 350:419-428.
53. Wang Q, Chen S, Jiang J, Liu J, Deng J, Ping X, Wei Z (2020) Chem Comm 56:2419-2422.
54. Delgado D, Soriano M, Solsona B, Zamora S, Agouram S, Concepción P, Nieto JL (2019) Appl Catal A: General 582:117092.
55. Deng Y, Lei H, Simon U, Ye D, Chen P (2023) ACS Catal 14:292-298.
56. Göltl F, Bhandari S, Lebrón-Rodríguez EA, Gold JI, Hutton DJ, Zones SI, Hermans I, Dumesic JA, Mavrikakis M (2024) Angew Chem Int Ed 63:e202403179.

Figures

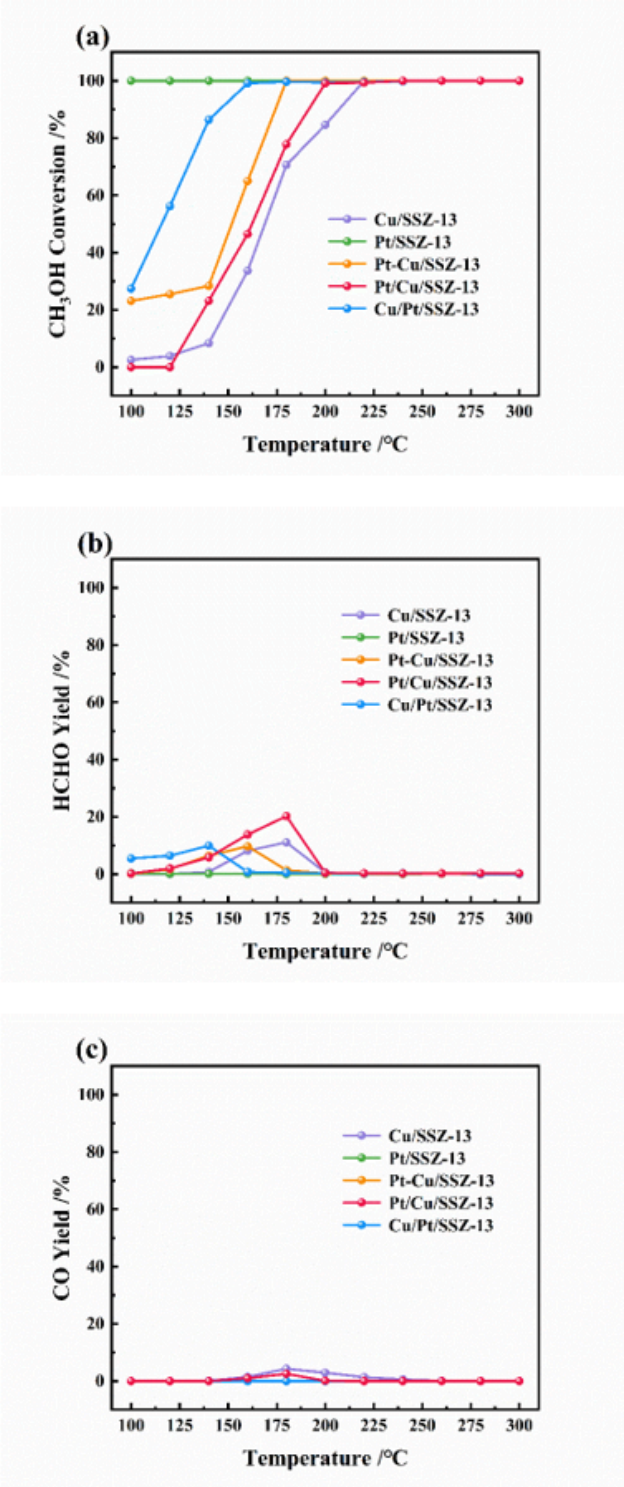


Figure 1

(a) CH_3OH conversion, (b) HCHO yield and (c) CO yield of all catalysts. (Reaction conditions: 0.2 mL catalyst, [CH_3OH] = 500 ppm, [O_2] = 5 vol.%, balance with N_2, total flow rate = 200 mL×min^{-1} and GHSV =60,000 h^{-1})

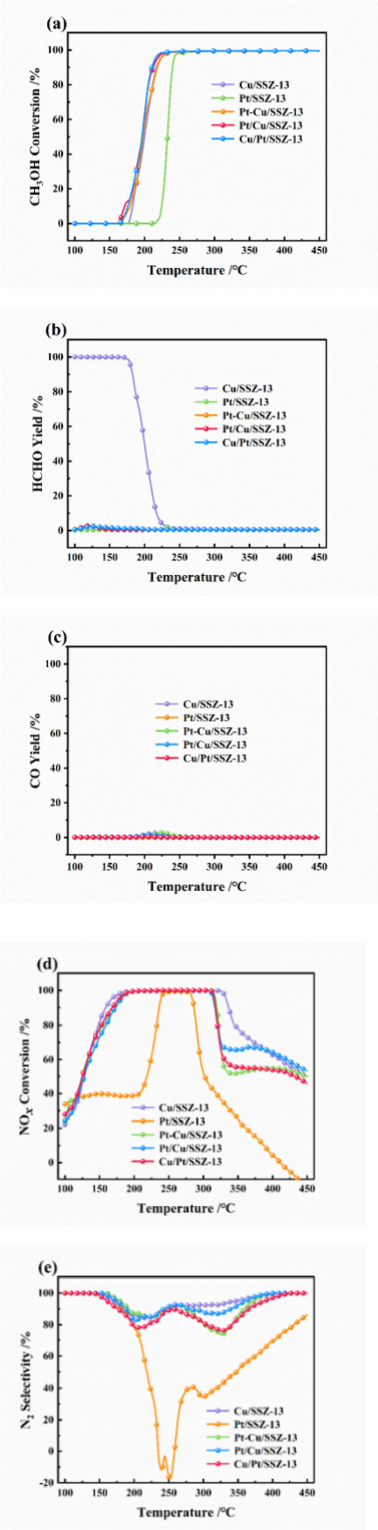


Figure 2

(a) CH_3OH conversion, (b) HCHO yield, (c) CO yield (d) NO_x conversion and (e) N_2 selectivity yield of all catalysts. (Reaction conditions: 0.2 mL catalyst, $[CH_3OH] = [NH_3] = [NO_x] = 500$ ppm, $[O_2] = 5$ vol.%, balance with N_2, total flow rate = 200 mL×min^{-1} and GHSV =60,000 h^{-1})

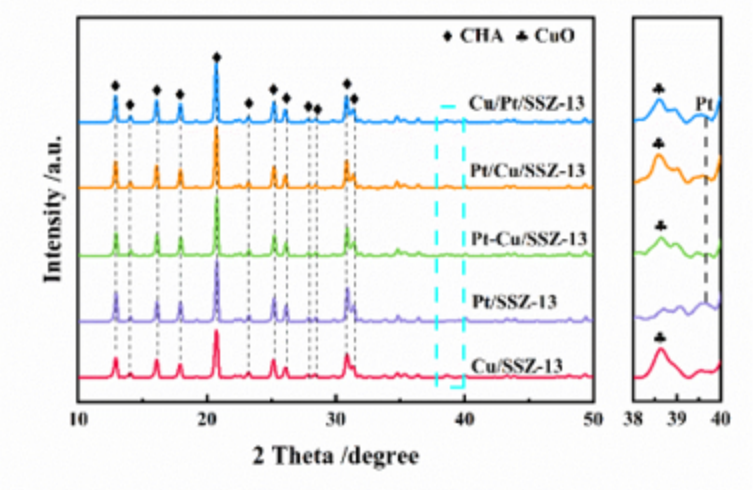


Figure 3

XRD patterns of different catalysts.

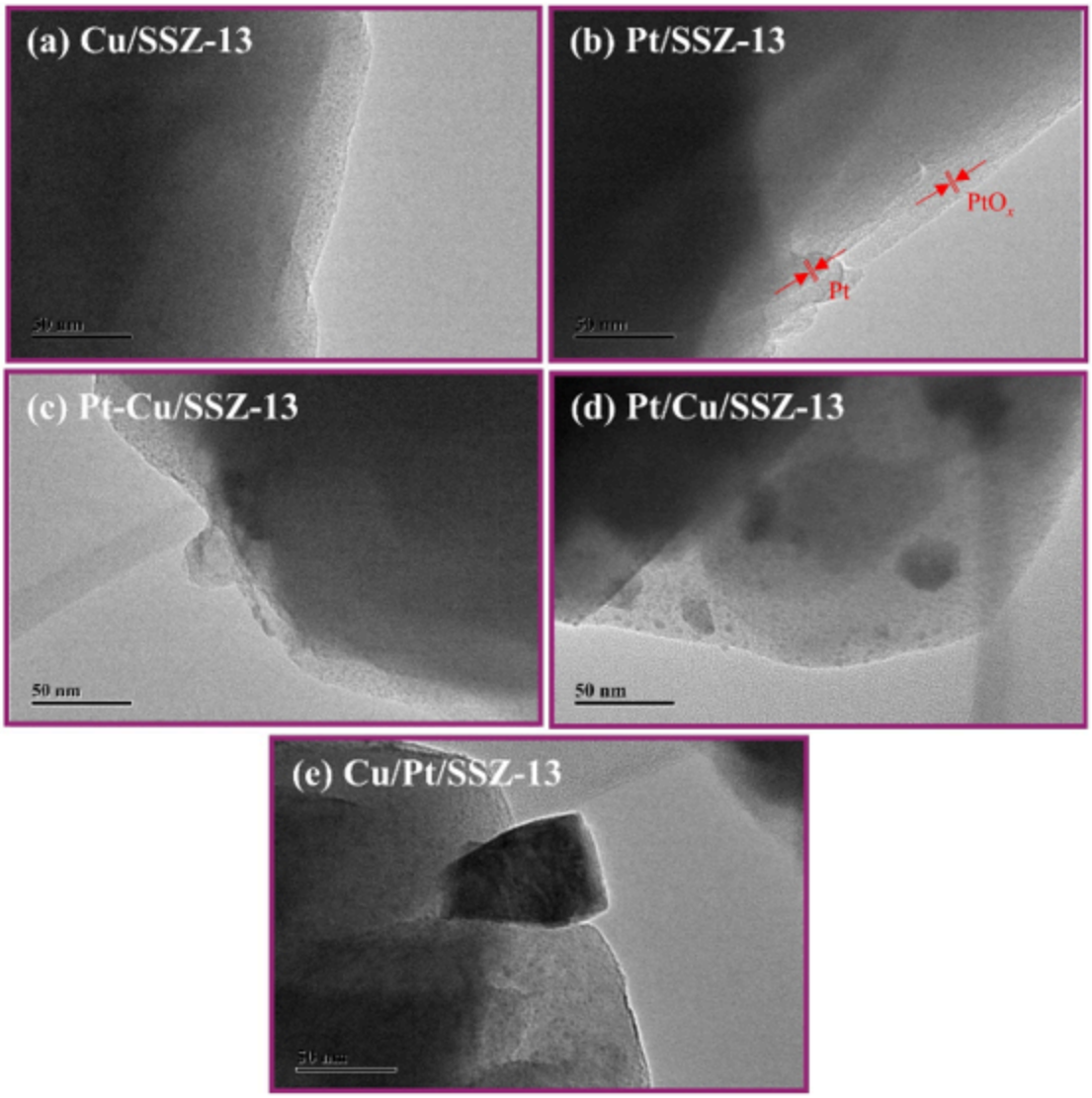


Figure 4

TEM images of (a) Cu/SSZ-13, (b) Pt/SSZ-13, (c) Pt-Cu/SSZ-13, (d) Pt/Cu/SSZ-13 and (e) Cu/Pt/SSZ-13 catalysts

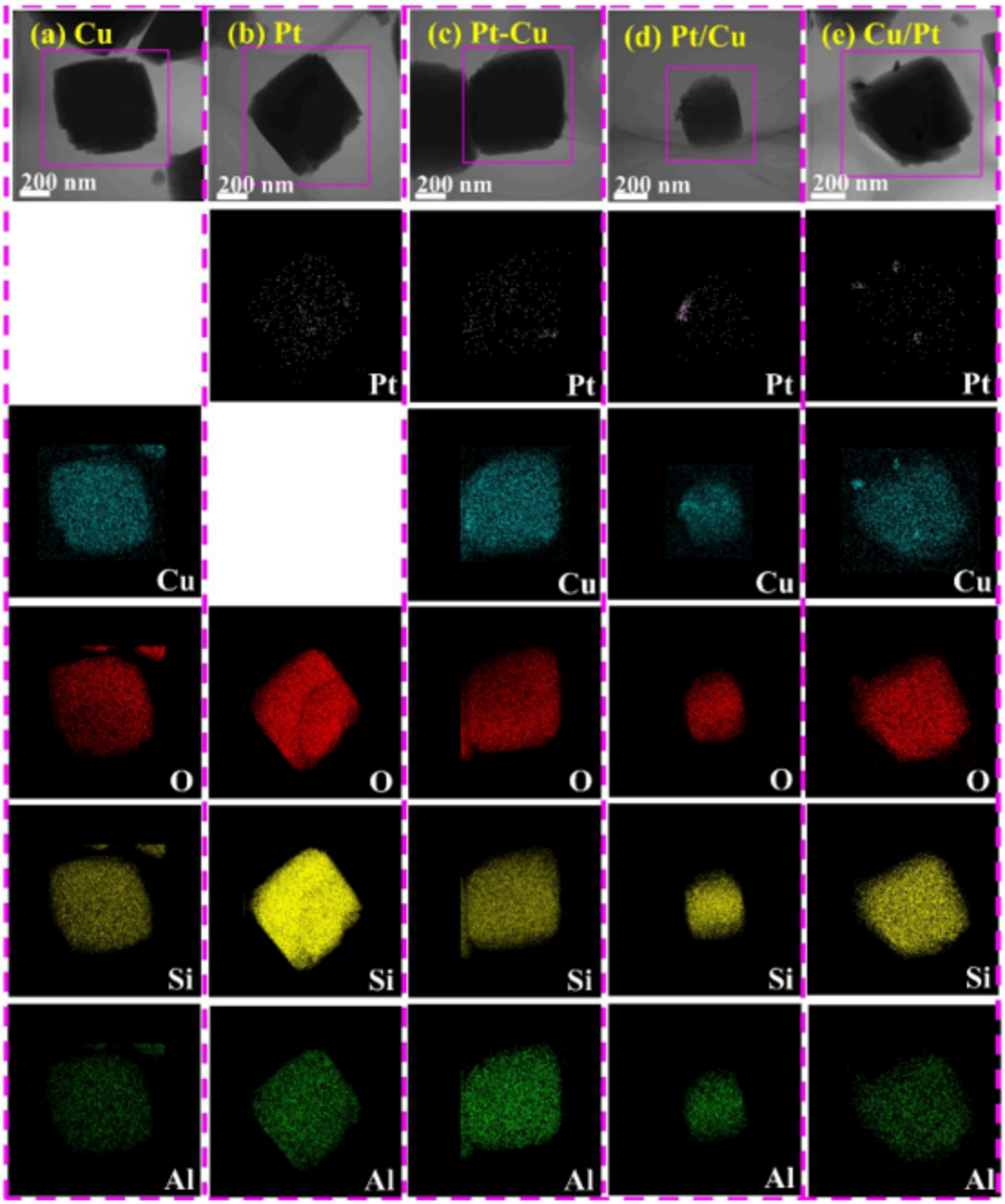


Figure 5

EDS images of (a) Cu/SSZ-13, (b) Pt/SSZ-13, (c) Pt-Cu/SSZ-13, (d) Pt/Cu/SSZ-13 and (e) Cu/Pt/SSZ-13 catalysts

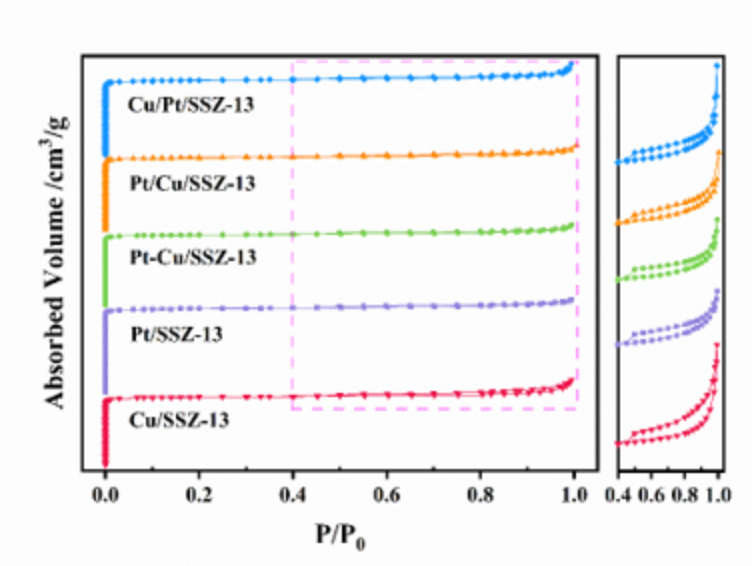


Figure 6

N_2 adsorption-desorption isotherms of different catalysts

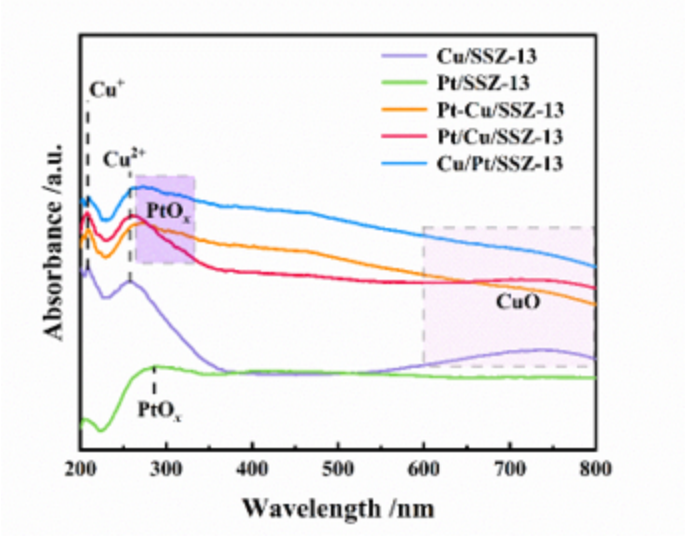


Figure 7

UV-Vis/DRS spectera of different catalysts in the range of 200-800 ºC.

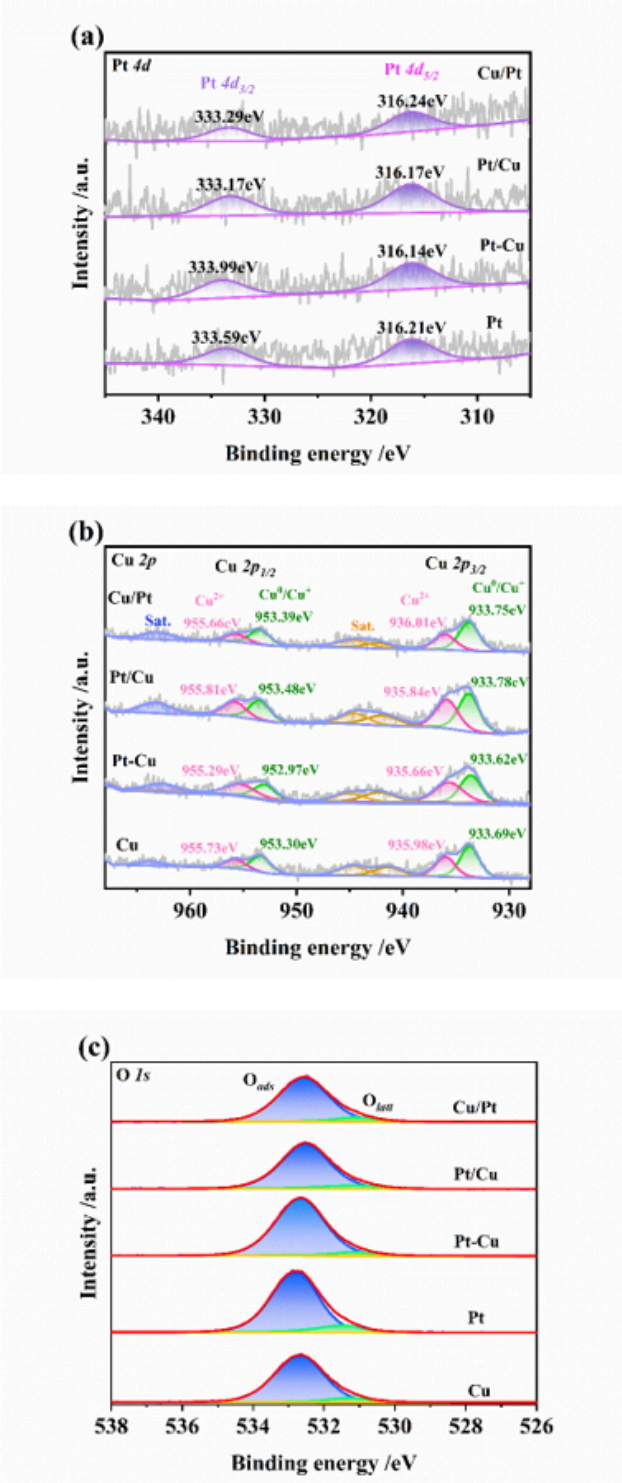


Figure 8

XPS spectra of (a) Cu 2*p*, (b) O *1s*over all catalysts.

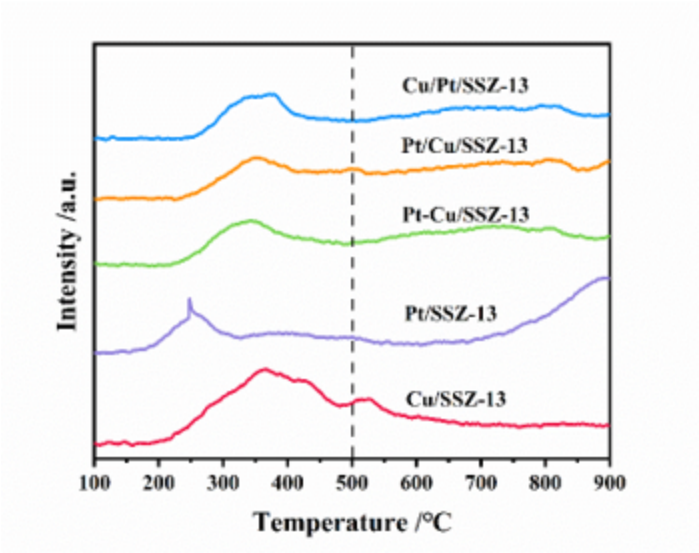


Figure 9

O_2-TPD profiles of all catalysts in the range of 100-900 °C.

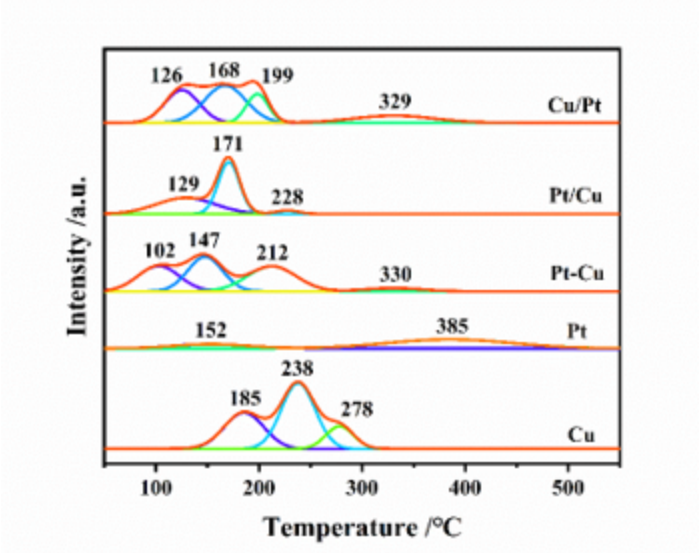


Figure 10

H_2-TPR profiles of all catalysts in the range of 100-800 °C.

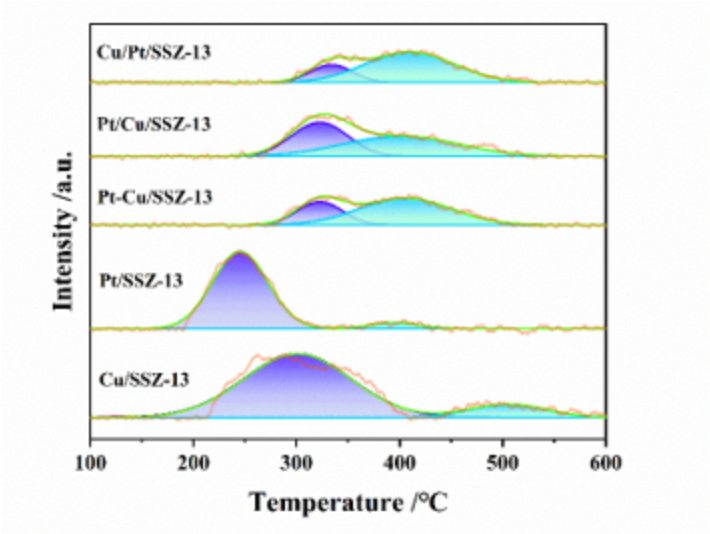


Figure 11

CO_2-TPD curves of all catalysts in the range of 100-500 °C.

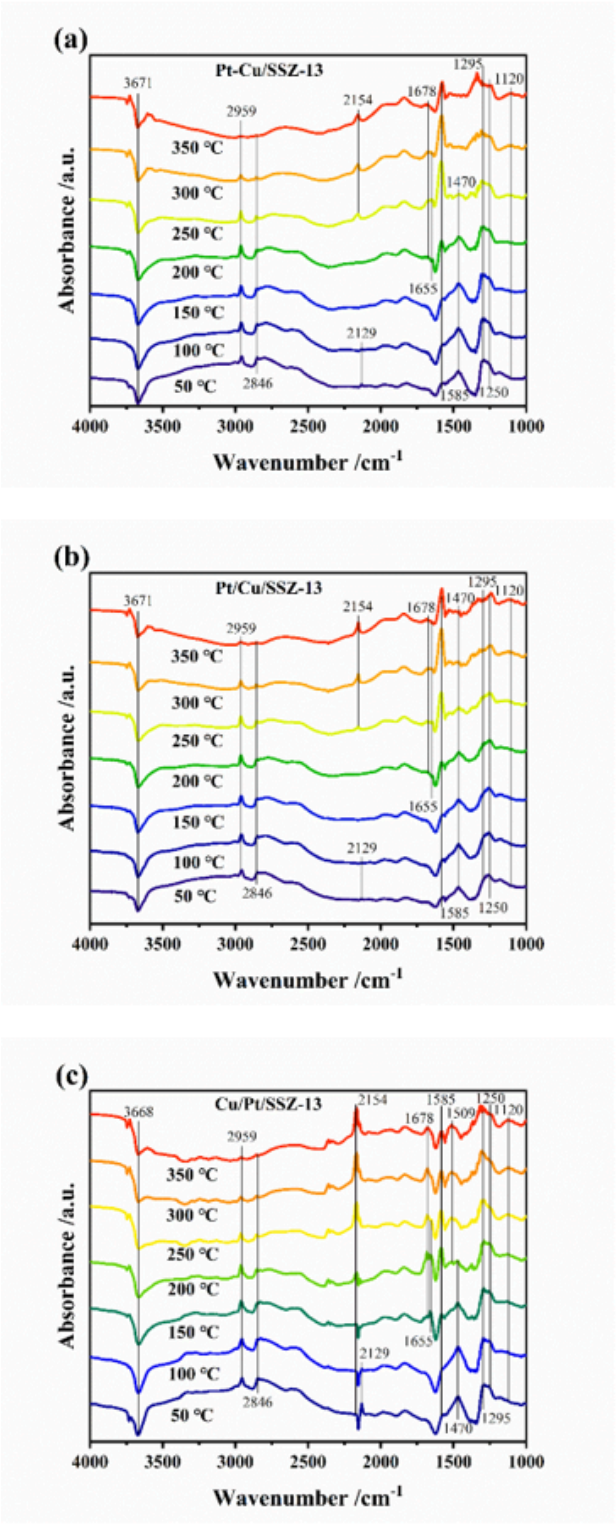


Figure 12

In-situ DRIFTS spectra of (a) Pt-Cu/SSZ-13, (b) Pt/Cu/SSZ-13 and (c) Cu/Pt/SSZ-13 catalysts at different temperatures. Condition: [CH_3OH] = 500 ppm, [O_2] = 5 vol.% and N_2 as balance gas

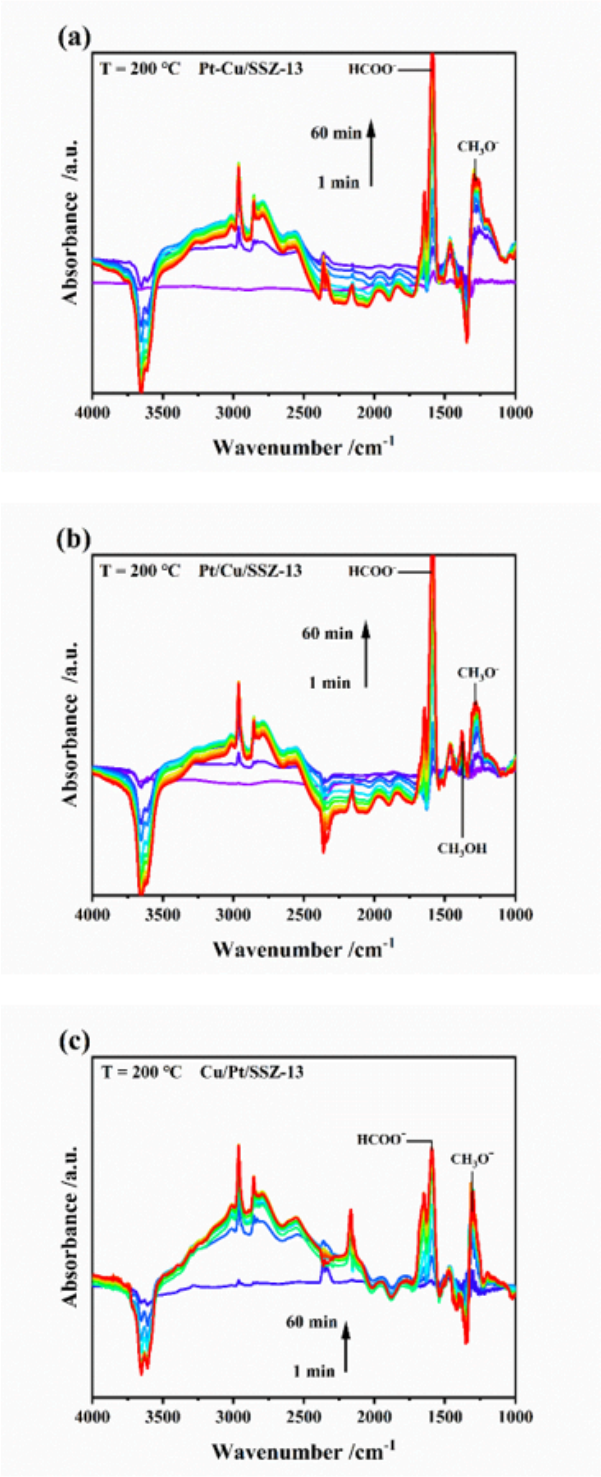


Figure 13

In-situ DRIFTS spectra of (a) Pt-Cu/SSZ-13, (b) Pt/Cu/SSZ-13 and (c) Cu/Pt/SSZ-13 catalysts at 200 °C. Condition: [CH_3OH] = 500 ppm, [O_2] = 5 vol.% and N_2 as balance gas

Supplementary Files

This is a list of supplementary files associated with this preprint. Click to download.

- Graphicalabstract.jpg
- SupportingInformation.docx